



Synthesis, characterization, and design of a photocatalyst based on BiOBr nanoplates and tin porphyrin with enhanced visible light photocatalytic activity

Marzieh Yaghoubi-berijani¹ · Bahram Bahramian¹ · Solmaz Zargari²

Received: 29 May 2019 / Accepted: 27 July 2019
© Springer Nature B.V. 2019

Abstract

The bismuth oxybromide (BiOBr) photocatalyst was first synthesized via a simple co-precipitation method. To improve the visible light photocatalytic activity of the prepared photocatalyst, it was then functionalized with the tin porphyrin (SnTCPP) photosensitizer to produce the modified photocatalyst BiOBr/SnTCPP. The modified photocatalyst produced was characterized by the X-ray powder diffraction, field emission scanning electron microscopy, UV–visible diffusive reflectance spectrometry, Fourier transform infrared spectrometry, Raman spectroscopy, and photoluminescence spectrometry analytical techniques. Furthermore, the photocatalytic activity of BiOBr/SnTCPP was evaluated for degradation of methyl orange (MO), Rhodamine B (RhB), and 2, 4-dichlorophenol (DCP). The photocatalytic results obtained showed that BiOBr/SnTCPP was able to destroy 78%, 90%, and 80% of MO, RhB, and DCP, respectively, under the visible light irradiation. The photocatalytic performance of BiOBr/SnTCPP was found to be much higher than that of BiOBr. In addition, investigating the photocatalytic mechanism by using some scavengers for photodegradation of the above-mentioned pollutants showed that the OH and O₂⁻ radicals were the main species involved in the photocatalytic process.

Keywords Bismuth oxyhalide · Tin porphyrin · Photodegradation · Visible light

✉ Bahram Bahramian
bahramian.b@shahroodut.ac.ir

¹ Faculty of Chemistry, Shahrood University of Technology, Shahrood, Iran

² Abadgaran Chemical Technology Development Research Group, Safadasht Industrial Complex, Safadasht, Shahriar, Iran

Introduction

With the progress of societies, the environmental issues, especially the presence of toxic organic materials in wastewaters, have received a considerable attention [1]. Water pollution is a major problem that has been increased drastically, causing global threats to the human beings and other living organisms. The pollutants are released fluently as wastes from the pharmaceutical, chemical, and other industries, leading to a decrease in the quality of water [2].

Sewage generated from the textile industry contains a large amount of azo dyes. Such colored dye sewages can threaten the surrounding ecosystems. The toxicity and potentially carcinogenic nature of these materials represent an increasing danger to life [3].

In order to solve such problems, the photodegradation of organic pollutants in nature through photocatalysis has received a considerable attention over the last few decades. Semiconducting photocatalysis has attracted an increasing attention as a promising environmentally friendly technology for wastewater remediation. Out of the different narrow band gap energy semiconductors, bismuth oxyhalides, BiOXs (X = Cl, Br, I), have shown striking photocatalytic activities under the visible light irradiation, which also has very interesting physical properties like a wide band gap energy [1, 4, 5].

BiOXs are a kind of newly exploited and efficient photocatalysts; they have become promising photocatalysts due to their special layered structure. Their uniquely layered structure is believed to improve the separation of photoinduced electron–hole pairs [6], and their light response can be tuned from the UV light to the visible light range, thus enhancing their photocatalytic performance. Furthermore, BiOXs are non-toxic and eco-friendly photocatalysts with low costs [7–10]. Therefore, BiOXs have attracted an increasing attention in practical industrial applications, especially the degradation of organic pollutants [11, 12], CO₂ conversion and Cr(VI) reduction [13] and in the fabrication of electrochemical cells [14].

BiOXs (BiOCl, BiOBr, and BiOI with the band gap energies of 3.2 eV, ~2.8 eV, and ~1.7 eV, respectively) [4, 15] are important semiconductors with an adjustable light responsive property by the halide ion. Presently, the unique performance of BiOXs in the photocatalytic degradation of organic compounds under both the UV and visible light irradiations has been given a great importance [16–18]. The photocatalytic performance of BiOXs strongly depends on their composition and microstructure [19, 20].

BiOXs, as Bi-based semiconductors, are of great importance for their electrical and optical properties and have exhibited excellent and promising applications as photocatalysts as well as sensors. All BiOX compounds are crystallized in a tetragonal matlockite structure [15, 21].

The main aim of this work was to ameliorate the photocatalytic activity of the synthesized BiOBr nanoplates in the visible light region. Various approaches have been proposed in order to activate the photocatalysts with a wide band gap energy in the visible light region such as the semiconductors doped with other

compounds like some metals and also sensitizing BiOBr with active compounds in the visible light region. Porphyrins and metalloporphyrins are among the strongest compounds used as a strong absorbent of the visible light. Porphyrins are attractive building blocks of organic macrocyclic compounds. Their 2D 18 π -electron aromatic macrocyclic compounds possess an excellent stability and unique optical, electronic, catalytic, and biochemical properties, and have been used in variant fields such as sensors, solar cells, biology, and catalysis [22–24]. ‘Pure’ porphyrins are not the best candidates as a photocatalyst because of their poor conductivity and high probability of electron–hole recombination [25]. In addition, these compounds are substantially stable in the presence of visible light. Porphyrins, due to their strong absorption of the visible light, are widely used in dye-sensitized solar cells. Sensitization of BiOXs by the porphyrin dyes is also considered as an effective approach to improve the visible spectral absorption and photocatalytic activity of BiOXs under the visible light irradiation.

In this work, we synthesized the BiOBr and BiOBr/SnTCPP photocatalysts. Firstly, the BiOBr nanoplates were prepared via a simple co-precipitation method and were then sensitized by the porphyrin dye SnTCPP. In order to fix the porphyrin dye on the surface of BiOBr via a strong chemical bonding, the synthesized modified photocatalyst BiOBr/SnTCPP was thoroughly characterized and its photocatalytic activity for degradation of the dyes such as methyl orange (MO), 2,4-dichlorophenol (DCP), and Rhodamine B (RhB) under an LED irradiation source was studied. In addition, the mechanism for the photocatalytic process was investigated and described.

Experimental

Materials

The reagents such as bismuth-(III) nitrate, potassium bromide, sodium acetate, nitric acid, pyrrole, propanoic acid, 4-carboxybenzaldehyde, pyridine, tin (II) chloride ($\text{SnCl}_2 \cdot 2\text{H}_2\text{O}$), *N,N*-dimethylformamide (DMF), and ethanol were supplied from the Merck Company and used without further purification. Deionized water was used to prepare all the solutions.

Instrumentation

The crystalline phase structure of the samples was determined by a D8-Advance Bruker using $\text{CuK}\alpha$ radiation ($\lambda=0.15406$ nm) at room temperature. The structural morphology of the samples was observed by a field emission scanning electron microscope, Zeiss SIGMA/VP (Germany). The UV–visible diffusive reflectance spectra (DRS) were taken using a Shimadzu MPC-2200 spectrophotometer. The Fourier transform infrared (FT-IR) spectra of the samples were taken using a Rayleigh spectrophotometer (China). The UV–visible spectra were obtained on a double-beam PerkinElmer spectrophotometer (America, lambda 360). The Raman

spectra were obtained on a uRaman-532-Ci Raman spectrometer from the Avantes Company (Netherlands). The photoluminescence spectra of the powdered samples were taken using a Shimadzu RF-6000 spectrofluorophotometer at an excitation wavelength of 200 nm. The lamp used in this work was a 5-W white LED (VF: 15–18 V, IF: 300 MA, TC: 600–8500 K) to provide visible light irradiation.

Synthesis of bismuth oxybromide (BiOBr)

In a typical experiment, in order to prepare the BiOBr sample, 0.01 mol $\text{Bi}(\text{NO}_3)_3$ powder was first dissolved in 15 ml HNO_3 (solution A). Solution B contained 0.01 mol KBr and 0.02 mol CH_3COONa in 100 ml distilled water. Solution A was added rapidly to solution B under vigorous stirring. The resulting white mixture was vigorously stirred for 12 h at room temperature for completion of the reaction. The resulting product was collected by centrifugation, washed for several times with water, and dried in an oven at 120 °C [26].

Synthesis of TCPP and SnTCPP

Tetrakis-(4-carboxyphenyl) porphyrin (TCPP) was synthesized according to the way they suggested in a paper [27]. For the synthesis of its tin complex, TCPP was dissolved in 100 mL pyridine, and the resulting solution was refluxed with the $\text{SnCl}_2 \cdot 2\text{H}_2\text{O}$ salt at 120 °C. The product obtained was washed with water and dried in an oven at 60 °C.

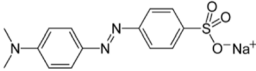
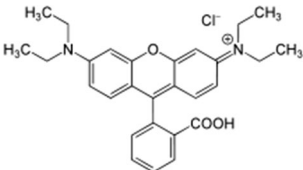
Photosensitization of BiOBr with SnTCPP

To photosensitize the prepared BiOBr nanoplates with SnTCPP, a mixture of BiOBr and SnTCPP (with the different weight ratios) was refluxed in 40 mL DMF at 150 °C. The synthesized product obtained was washed with DMF and water and was subsequently dried in an oven at 60 °C [27].

Photodegradation process

To examine the photocatalytic activity of the prepared photocatalysts BiOBr and BiOBr/SnTCPP, the photodegradation of the colored contaminants MO (pH=3), DCP, and RhB (Table 1) with a concentration of 10 mg L^{-1} was investigated in the presence of the photocatalysts with a concentration of 0.6 g L^{-1} under the visible light irradiation; a 5-W white LED lamp was used as the visible light source. A mixture of the organic pollutants and a photocatalyst was stirred in the dark for 30 min to achieve an adsorption–desorption equilibrium between the organic pollutants and the photocatalyst. All the photocatalytic experiments were carried out under the same conditions at room temperature. At defined intervals (1 h), ca. 3 mL of the mixture was centrifuged, and then, the spectral absorption changes for MO, DCP, and RhB were measured at 506 nm, 284 nm, and 552 nm, respectively, to monitor the photodegradation processes.

Table 1 Physicochemical properties of the understudied organic pollutants

Organic pollutant	Chemical formula	Chemical structure	Molar mass (g mol ⁻¹)
MO	C ₁₄ H ₁₄ N ₃ NaO ₃ S		327.33
RhB	C ₂₈ H ₃₁ ClN ₂ O ₃		479.02
DCP	C ₆ H ₄ Cl ₂ O		163.00

Results and discussion

Structural and morphological analyses

FT-IR analysis

The FT-IR spectra shown in Fig. 1 confirm the chemical structures of BiOBr and BiOBr/SnTCPP. In these spectra, the vibration peak for the metal–oxygen bond (Bi–O) appears at about 511 cm⁻¹, and the same peak can be observed in the BiOBr/SnTCPP photocatalyst, which indicates the existence of BiOBr, as expected [28, 29].

Figure 1a, b shows the structure and FT-IR spectra for SnTCPP–Cl₂.

In the FT-IR spectra for SnTCPP–Cl₂ shown in Fig. 1b, a strong C=O stretching band could be observed at around 1703 cm⁻¹. Two weak C–O peaks appeared at 1402 and 1276 cm⁻¹, which could be attributed to the anti-symmetric and symmetric stretches of the –COO⁻ functional group present in SnTCPP–Cl₂. The peak at 1606 cm⁻¹ can be assigned to C=C stretching of the benzenoid rings. Also, the peak at 565 cm⁻¹ can be assigned to the Sn–Cl bond, confirming the presence of the axial Cl ligands in SnTCPP–Cl₂.

After the SnTCPP molecules were fixed on the surface of BiOBr (Fig. 1b), a strong C=O stretching band could be observed around at 1700 cm⁻¹. Also, the peak at 1602 cm⁻¹ could be assigned to the C=C stretching of the benzenoid rings. In the spectrum for the BiOBr/SnTCPP photocatalyst, the defined peak for the C=O group at 1700 cm⁻¹ shows that SnTCPP is located on the surface of the nanoplates. Also, in the BiOBr/SnTCPP spectrum, the characteristic peak for the Sn–Cl bond was removed, which confirmed the connection of SnTCPP through the tin atom on the surface of the BiOBr nanoplates.

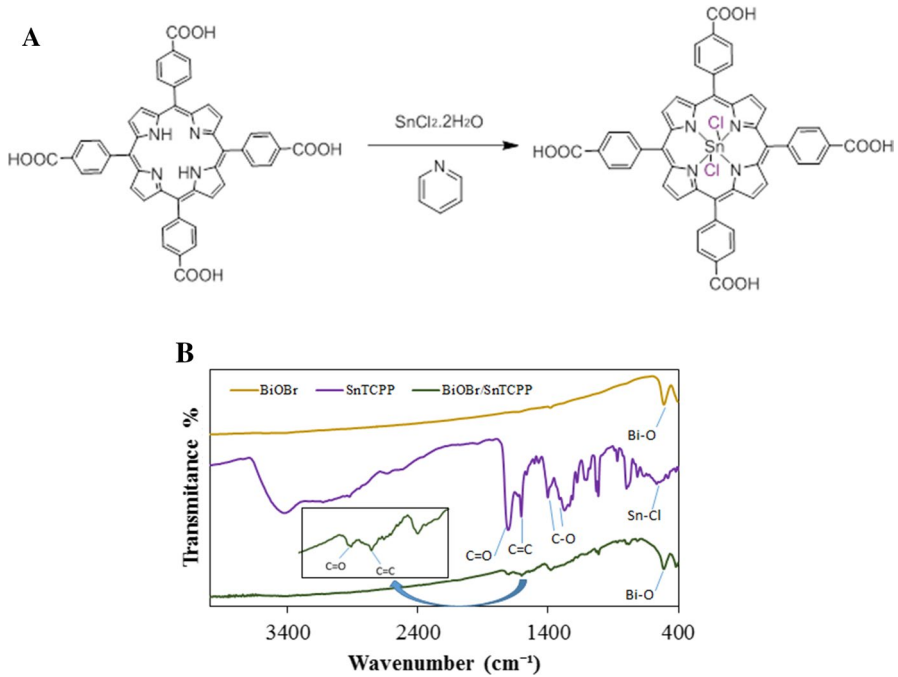


Fig. 1 **a** Structure of as-prepared SnTCPP-Cl₂ and **b** FT-IR spectrum for the samples

UV–visible diffuse reflectance spectra

Figure 2 shows the UV–visible diffuse reflection spectra for the BiOBr nanoplates. As it is evident in this figure, the spectrum for pure BiOBr powder clearly shows an absorption edge at 440 nm.

The band gap energy of a semiconductor is important in determining its photocatalytic activity and thus worth investigating. The relationship between the absorbance and the incident photon energy $h\nu$ can be described as:

$$Ah\nu = C(h\nu - E_g)^{1/2}$$

where h , A , E_g , and ν represent the Planck constant, absorption coefficient, band gap energy, and incident light frequency, respectively, and C denotes a constant. The band gap energy for the synthesized photocatalysts could be estimated from a plot depicting $(Ah\nu)^2$ versus $h\nu$ (Fig. 2c). The intercept of the tangent to the X-axis gives rise to a good approximation of the band gap energies for BiOBr and BiOBr/SnTCPP; the band gap energy for the BiOBr nanoplates was estimated to be almost 2.8 eV. The SnTCPP spectrum exhibited a Soret band at 400 nm and two Q bands in the 558 and 602 nm (Fig. 2a).

As shown in Fig. 2b, BiOBr/SnTCPP exhibits a visible light absorption in the range of 400–700 nm. Consequently, BiOBr/SnTCPP exhibited a broader absorption range in the solar spectrum than BiOBr. The BiOBr/SnTCPP spectrum exhibited a

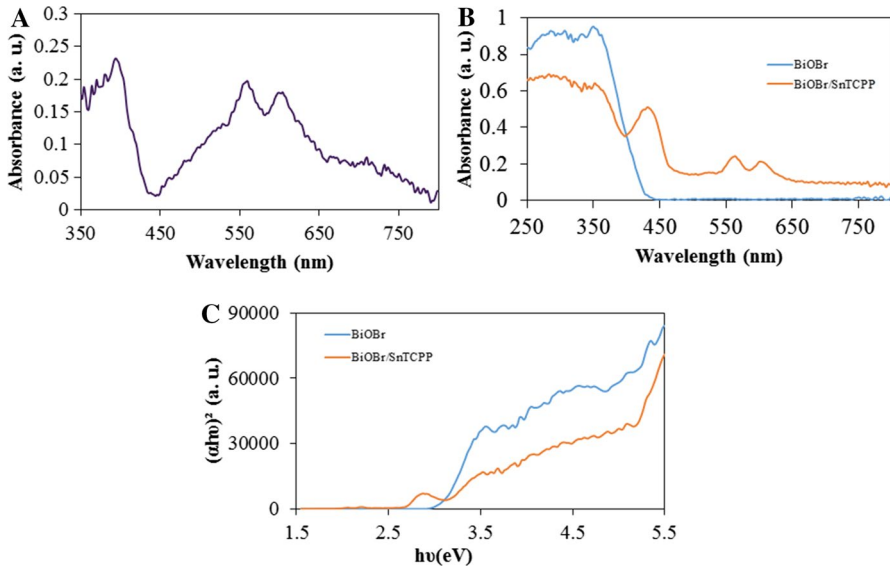


Fig. 2 UV-visible diffusive reflectance spectra for **a** SnTCPP and **b, c** BiOBr and BiOBr/SnTCPP photocatalysts

Soret band at 434 nm and two Q bands in the range of 566–606 nm. The presence of these characteristic peaks for porphyrin in the diffusive reflectance spectrum for BiOBr/SnTCPP is an evidence for the existence of SnTCPP in BiOBr/SnTCPP. Furthermore, the absorbance of BiOBr/SnTCPP in the visible light region was increased relative to BiOBr, which might be due to the high porphyrin ability in absorbing the visible light. These results indicate the photosensitizing process, with porphyrin forming an efficient approach to increase the BiOBr photocatalytic activity under the visible light irradiation [27].

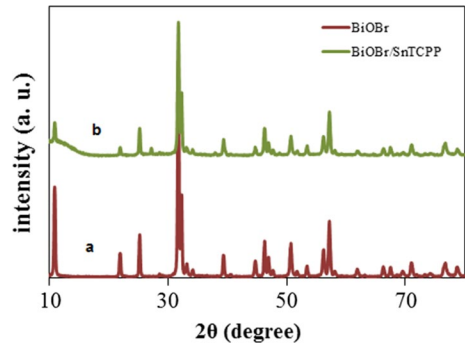
X-ray diffraction (XRD) analysis

The crystallographic structure and phase purity of the prepared photocatalysts were examined by XRD analysis. Figure 3 shows the XRD patterns for BiOBr and BiOBr/SnTCPP.

The observed diffraction peaks at $2\theta = 10.76^\circ$, 21.8° , 25.08° , 31.56° , 31.92° , 39.2° , 46.16° , 50.52° , and 57.08° correspond to the planes of (001), (002), (001), (012), (110), (112), (020), (014), and (212), respectively, in the order that can be readily indexed to the tetragonal phase of BiOBr with the lattice parameters $a = b = 3.926 \text{ \AA}$ and $c = 8.103 \text{ \AA}$ [space group: $P4/nmm$] (corresponding to the JCPDS File No. 73-2061) [26]. The strong and sharp peaks in the XRD pattern for BiOBr indicate that it is well crystallized.

Characterizations of BiOBr/SnTCPP are shown in Fig. 3, in which it can be seen that there is no significant change in the XRD pattern for BiOBr/SnTCPP compared

Fig. 3 XRD patterns for (a) BiOBr and (b) BiOBr/SnTCPP



to that for pure BiOBr. Therefore, BiOBr functionalization with SnTCPP had little effect on the inter-layer spacing and structure of BiOBr.

Raman spectra

In the Raman spectra for BiOBr (Fig. 4), the strong peaks at 126 cm^{-1} can be assigned to the A_{1g} stretching vibration of the Bi–Br bond, the peak at 154 cm^{-1} can be attributed to the E_{2g} stretching vibration of the Bi–Br bond, and the peak at 370 cm^{-1} is caused by the vibration of the Bi–O bond [30, 31]. The above-mentioned observations could further confirm that the understudied sample was indeed BiOBr.

In Fig. 4, the Raman spectroscopy of SnTCPP indicates the important role of vibronic effects. Also show that these terms play a predominant role in inducing hot difference bands corresponding to resonance Raman transitions between fundamental levels of vibrational modes of different symmetry. In the range of $1300\text{--}1590\text{ cm}^{-1}$, the spectra bands are assigned to the C–C bond stretching [32]. The observed Raman band at 1589 cm^{-1} are vibrational stretching of the phenyl rings [33].

The Raman spectra for the BiOBr/SnTCPP photocatalyst also show the above-mentioned peaks with weak intensities, which could be due to the covering of the

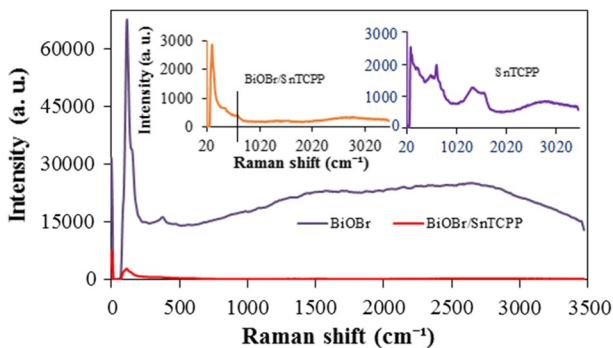


Fig. 4 Raman spectra for the SnTCPP, BiOBr, and BiOBr/SnTCPP photocatalyst samples

BiOBr peaks with the SnTCPP ones. Also, in the Raman spectra of BiOBr/SnTCPP, the peaks are shifted to a lower frequency. The peak at 605 cm^{-1} can be attributed to SnTCPP, which could be due to the connection of SnTCPP to BiOBr.

Photoluminescence (PL) spectra

It is well known that a photocatalytic activity is usually perfected by the photogenerated electrons and holes. Thus, to further explain the separation efficiency of the charge carriers, the PL spectra for BiOBr and BiOBr/SnTCPP were studied to appraise the segregation efficiency of the photoinduced charge carriers [34].

The PL emissions (Fig. 5) of BiOBr and BiOBr/SnTCPP were characterized using the 200 nm excitation wavelength. The powdered samples were used without further treatment. As indicated in Fig. 5, the main emission peaks were centered at 435–520 and 625 nm for BiOBr [35]. The emission intensity of pure BiOBr is the highest; this intensity also elucidates a higher carrier recombination occurring for BiOBr [36].

The PL intensity of the BiOBr/SnTCPP photocatalyst is low. A lower PL intensity usually indicates a higher segregation efficiency of the photoinduced charges and thus a higher photocatalytic activity [37, 38].

FE-SEM images

The morphologies of the samples SnTCPP, BiOBr, and BiOBr/SnTCPP were examined by field emission scanning electron microscopy (FE-SEM). As it is shown in Fig. 6a, SEM shows isolated tin porphyrin aggregates with sizes in the nanometer range.

The BiOBr sample is composed of a large amount of relatively uniform plates. Furthermore, it can be clearly seen that the surface of the BiOBr nanoplates is flat and smooth. Some plates aggregate into a flower-like cluster. A unique nanoplate morphology with an average diameter of approximately 20–50 nm can be clearly observed (Fig. 6b).

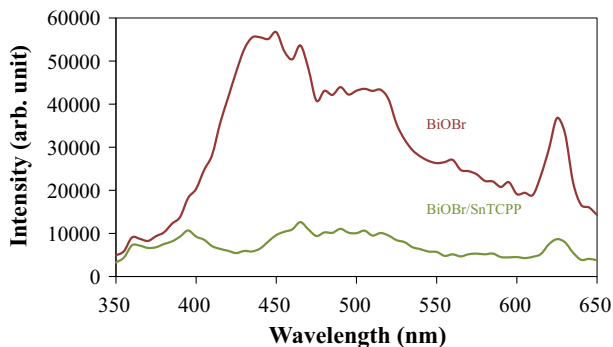


Fig. 5 PL spectra for BiOBr and BiOBr/SnTCPP with an excitation wavelength of 200 nm

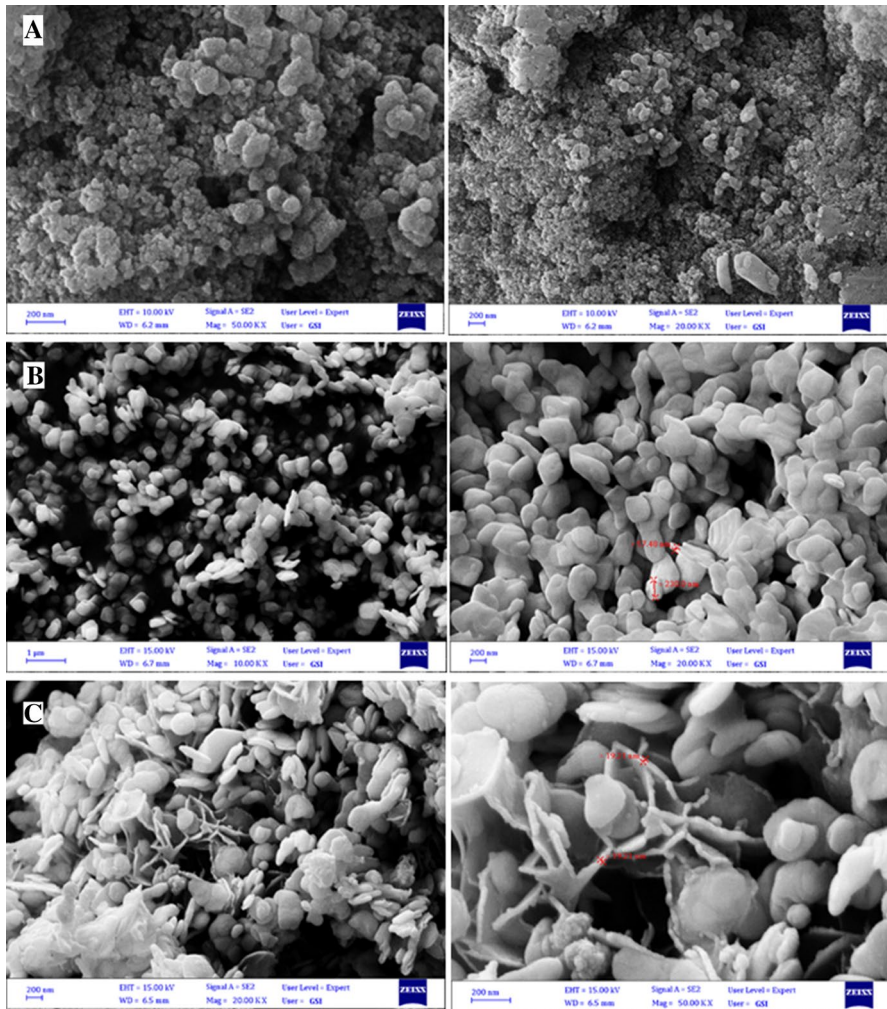


Fig. 6 SEM images for a SnTCPP, b BiOBr, c BiOBr/SnTCPP, elemental mapping, d SnTCPP, and e BiOBr/SnTCPP

Taking into account the evolution of the surface area of BiOBr, the structure and morphology of the BiOBr nanoplates were discussed. A modification in the activity betterment of BiOBr could increase its photocatalytic activity [39].

As shown in Fig. 6c, the surface of BiOBr nanoplates is attached to the SnTCPP nanoparticles, and the good contact between the two compounds is thought to promote the transfer of the photoinduced carriers from SnTCPP to BiOBr. The nano-surface structure of BiOBr/SnTCPP is similar to that for BiOBr, and it appears to be stacked by SnTCPP, but the thickness of BiOBr is relatively narrow.

In the BiOBr/SnTCPP photocatalyst, an intercalation between SnTCPP and BiOBr is formed through the Bi–O–Sn–O–Bi bonding. This bonding is formed

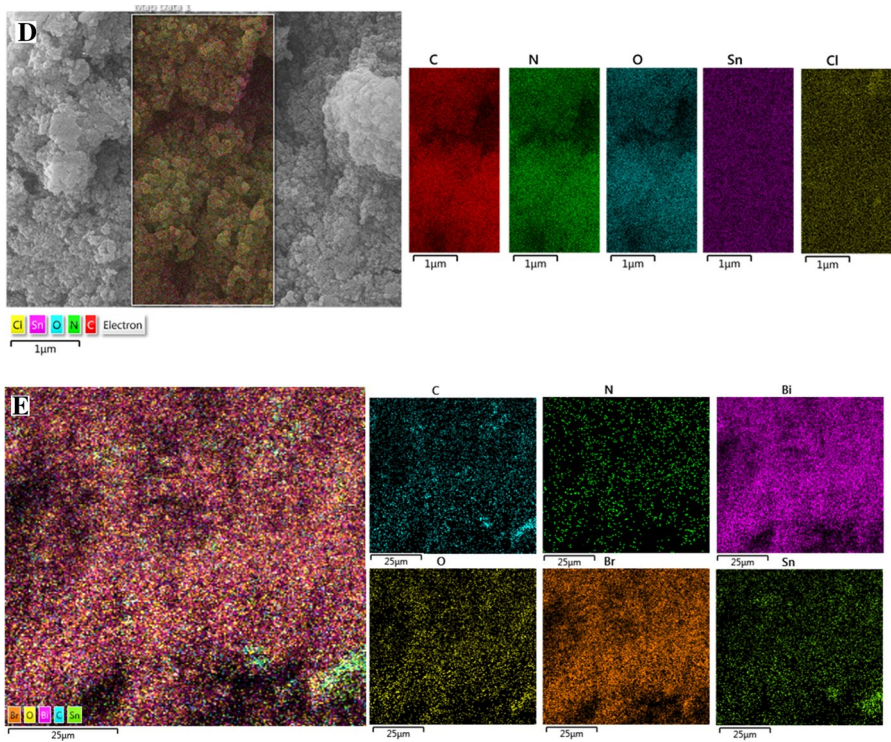


Fig. 6 (continued)

through the metal–ligand axial coordination to the surface hydroxyl groups of the BiOBr nanoplates [40]. To indicate the elemental mapping of the SnTCPP and BiOBr/SnTCPP photocatalyst, elemental mapping was performed. The elemental mapping of SnTCPP shows a distribution of the elements of C, O, N, Cl, and Sn (Fig. 6d).

As indicated in the corresponding elemental mapping of BiOBr/SnTCPP photocatalyst (Fig. 6e), Bi, O, Br, C, N, and Sn elements are clearly distributed. On the basis of the elemental mapping, the presence of element Sn indicates the photosensitization of BiOBr nanoplates with SnTCPP.

Photocatalytic activities of BiOBr and BiOBr/SnTCPP

Photodegradation of MO, DCP, and RhB

To further evaluate the photocatalytic performance of BiOBr and BiOBr/SnTCPP, a series of experiments were carried out for the photodegradation of the understudied organic pollutants under the visible light irradiation. Figure 7 shows the photocatalytic efficiencies of BiOBr and BiOBr/SnTCPP. RhB and MO are the two kinds of organic azo dyes that are often used as model pollutants to study the photocatalytic

Fig. 7 Photocatalytic degradation efficiencies of **a** BiOBr and **b** BiOBr/SnTCPP (10:1) (MO), **c** BiOBr/SnTCPP with different ratios, **d, e** photocatalytic degradation efficiencies of DCP and RhB for BiOBr/SnTCPP (10:1); kinetics of **f** MO, **g** DCP and **h** RhB using BiOBr and BiOBr/SnTCPP under the visible light irradiation

performance of the photocatalysts. In this work, RhB, MO, and DCP were chosen as the target pollutants to trace the photocatalytic activities of BiOBr and BiOBr/SnTCPP under the visible light irradiation.

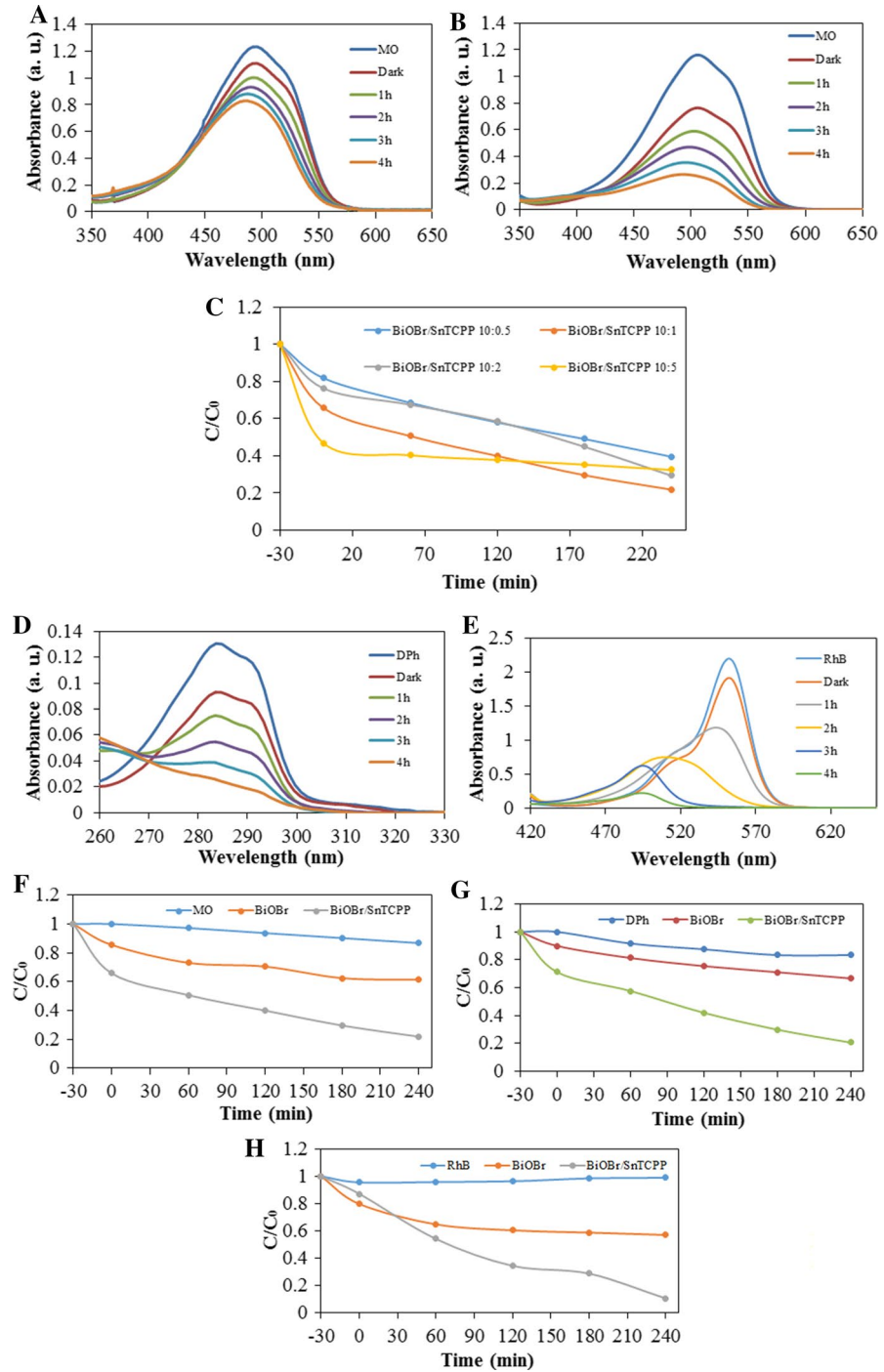
Figure 7f shows the variation in the MO concentration with the irradiation time over the BiOBr and BiOBr/SnTCPP photocatalysts. As a comparison, the direct photolysis of MO was performed under the identical conditions. We observed that the photolysis of MO was negligible under the visible light irradiation. The degradation of MO by BiOBr was about 38% (Fig. 7a). The photocatalytic activity of the prepared samples was evaluated for the photodegradation of MO, and the results are presented in Fig. 7b. It is shown in Fig. 7b that the photodegradation efficiency of MO for the BiOBr/SnTCPP photocatalysts enhances compared with BiOBr. For comparison, the BiOBr/SnTCPP photocatalysts with different weight ratios (10:0.5, 10:1, 10:2 and 10:5) were designed and the results were calculated 60%, 78%, 70% and 62.5%, respectively (Fig. 7c). A suitable amount of SnTCPP might increase an efficient absorption of light in the visible region and help the separation and transportation of induced charge carriers, leading to an improved photocatalytic activity. The decrease in the photocatalytic performance at a high SnTCPP loading may be because of the inhibition of the light arriving at the catalyst surface.

The photocatalytic activity of BiOBr/SnTCPP was evaluated for the degradation of DCP under the visible light irradiation. The experimental results obtained for the DCP degradation are displayed in Fig. 7d, g. The results shown in Fig. 7g revealed that around 33% and 80% of DCP were degraded by BiOBr and BiOBr/SnTCPP, respectively.

Figure 7e, h shows the photocatalytic degradation of RhB on the BiOBr/SnTCPP photocatalysts. The degradation of RhB by BiOBr and BiOBr/SnTCPP was about 43% and 90%, respectively. Under the visible light irradiation, the BiOBr/SnTCPP photocatalyst showed a much better photocatalytic activity than BiOBr alone.

Photocatalytic mechanism

In order to investigate the photocatalytic mechanism for the photocatalytic activity of the BiOBr/SnTCPP photocatalyst, the photodegradation of MO was conducted using various scavengers like AgNO_3 (2 mmol) as an electron scavenger, *tert-butyl* alcohol (*tert*-BuOH, 1 mmol) and methanol (MeOH, 1 mmol) as OH radical scavengers, in the absence of O_2 (N_2 saturation condition) to investigate the superoxide anion radical (O_2^-) generation and disodium ethylenediaminetetraacetic acid (Na_2EDTA , 2 mmol) as a hole (h^+) scavenger. As it is seen in Fig. 8, *tert*-BuOH, MeOH, Na_2EDTA , and N_2 inhibited the photocatalytic activity of BiOBr/SnTCPP. This could be resulted from the generation of OH and O_2^- radicals in the photocatalytic process. Observation of the photodegradation of the understudied pollutants



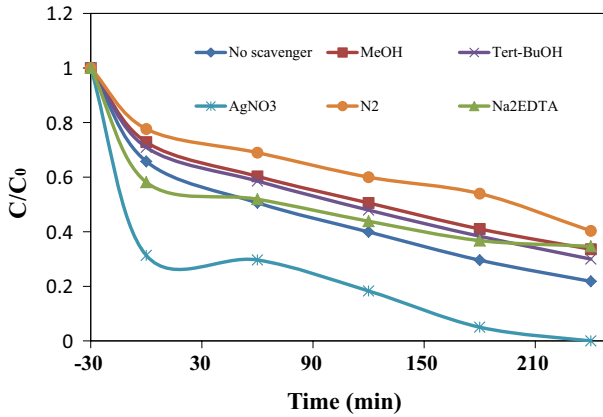


Fig. 8 Photocatalytic mechanism of BiOBr/SnTCPP in the presence of different scavengers

with BiOBr/SnTCPP indicates that the OH and O_2^- radicals are the main species involved in the photodegradation process.

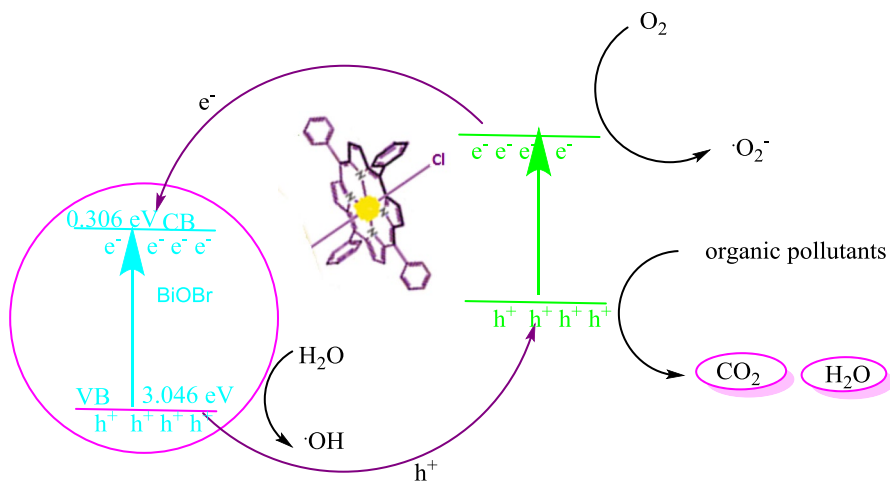
It attracts one's attention that the photodegradation performance was improved with the addition of $AgNO_3$. This phenomenon is very likely to be related to the accelerated use of e^- by addition of the scavengers of $AgNO_3$, which efficiently improve the rate of separation of electrons and holes, resulting in an increased degradation rate [41, 42].

Description of photocatalytic activity

The photocatalytic activity of the semiconducting photocatalysts depends on several factors such as their crystallinity, surface structure, surface area, and band gap energy. The BiOBr nanoplates induce a rapid generation of radical species under the visible light irradiation. The activity of the BiOBr nanoplates is due to the formation of a non-faceted morphology comprising a high surface area and a small crystallite size distribution [43, 44].

The schematic charge transfer and enhanced photoactivity of BiOBr photosensitized with SnTCPP are shown in Scheme 1.

In the photocatalyst BiOBr/SnTCPP, due to the presence of two axial chlorine ligands in SnTCPP- Cl_2 , the bond between BiOBr and SnTCPP is established through the interaction between the chlorine ligands in SnTCPP- Cl_2 and the OH groups present on the surface of BiOBr. The presence of this connection as well as the central metal atom is very important in the transfer of electrons from porphyrin to the BiOBr semiconductor. The electron transfer has a significant effect on the photodegradation of pollutants. In this photocatalyst, the electrons excited in porphyrin are transmitted through the axial connections to BiOBr, and SnTCPP acts as a channel in this electron transfer process. The presence of axial ligand connections is very effective in the process of electron transfer from the metal atom in the center of the porphyrin ring to BiOBr.



Scheme 1 Schematic illustration of charge transfer in the photocatalytic degradation of BiOBr/SnTCPP [36, 45]

Photocatalyst stability and reuse

The important characteristics of an efficient photocatalyst are its easy recovery, resistance to light, and long lifetime. After completion of the photodegradation of MO, the BiOBr/SnTCPP photocatalyst was separated, washed with acetone and water, and dried in an oven. The FT-IR and UV–visible diffusive reflectance spectra for BiOBr/SnTCPP confirm the presence of SnTCPP on the BiOBr/SnTCPP photocatalyst (Fig. 9). As shown in Fig. 10, the photocatalyst was then collected and reused to assess its performance in a new cycle of photodegradation of MO. In the second, third, and fourth tests, the rate of MO degradation exhibited a low decrease as a result of a smaller quantity of the recovered photocatalyst. It could be seen that even after 4 cycles, more than 72% MO was photodegraded.

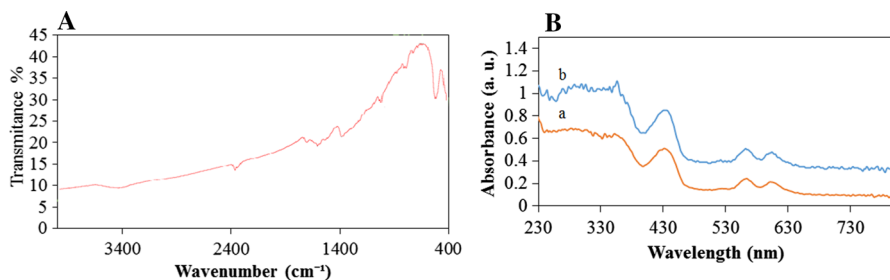


Fig. 9 **a** FT-IR spectra for BiOBr/SnTCPP after the reaction and **b** diffusive reflectance spectra for BiOBr/SnTCPP (a) before and (b) after MO degradation

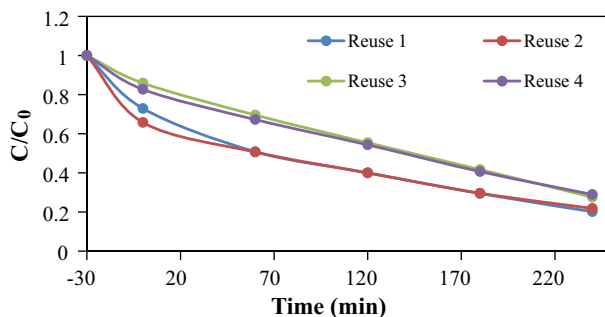


Fig. 10 Recycling tests for photodegrading MO using the BiOBr/SnTCPP photocatalyst

Conclusions

In order to improve the visible light efficiency of the prepared BiOBr photocatalyst for its photocatalytic activity, it was functionalized with the tin complex of porphyrin photosensitizer (SnTCPP). The new photocatalyst BiOBr/SnTCPP was successfully prepared through a simple method.

The as-prepared BiOBr/SnTCPP photocatalyst showed a much better visible light absorption in the photocatalytic degradation of RhB, MO, and DCP. BiOBr/SnTCPP exhibited an excellent photocatalytic activity and a higher stability than BiOBr. The better photocatalytic performance of BiOBr/SnTCPP was strongly affected by its crystallite size and morphology. A better photocatalytic performance was achieved for BiOBr/SnTCPP with a nanoplate morphology. With a low-intensity lamp (5 W), the conversion rate for degradation of the understudied colored dyes was about 60–80% after 4 h of irradiation. As expected, the new photocatalyst BiOBr/SnTCPP not only had higher photodegradation efficiency than pure BiOBr but also had an excellent photostability for photodegradation under the visible light irradiation. Also, the sensitization of BiOBr with SnTCPP was increased by about 50% in photodegradation compared to BiOBr (38%). This is because the energy level of the excited SnTCPP and the CB of BiOBr is properly overlapped, which led to a decrease in the recombination of the electron–hole pair, and thus promoted the photodegradation efficiency. The above-mentioned results clearly stated that MO was degraded by the active hydroxyl species and superoxide anion radicals. The results obtained indicate that the BiOBr nanoplates can be further studied as a promising visible light active support for SnTCPP in the photoassisted solar energy conversion applications.

Acknowledgements The authors wish to thank the Vice-President's Office for Research Affairs in the University of Shahrood for supporting this work.

References

1. Q. Wang, D. Jiao, J. Lian, Q. Ma, J. Yu, H. Huang, J. Zhong, J. Li, *J. Alloy. Compd.* **649**, 474 (2015)
2. K. Natarajan, H.C. Bajaj, R.J. Tayade, *J. Ind. Eng. Chem.* **34**, 146 (2016)
3. Y. Zhiyong, D. Bahnemann, R. Dillert, S. Lin, L. Liqin, *J. Mol. Catal. A: Chem.* **365**, 1 (2012)
4. X. Shi, P. Wang, W. Li, Y. Bai, H. Xie, Y. Zhou, L. Ye, *Appl. Catal. B Environ.* **243**, 322 (2019)

5. Y. Bai, T. Chen, P. Wang, L. Wang, L. Ye, *Chem. Eng. J.* **304**, 454 (2016)
6. Y. Zhao, X. Huang, X. Tan, T. Yu, X. Li, L. Yang, S. Wang, *Appl. Surf. Sci.* **365**, 209 (2016)
7. H. Cheng, B. Huang, Z. Wang, X. Qin, X. Zhang, Y. Dai, *Chem. A Eur. J.* **17**, 8039 (2011)
8. J. Jiang, K. Zhao, X. Xiao, L. Zhang, *J. Am. Chem. Soc.* **134**, 4473 (2012)
9. Z. Jiang, B. Huang, Z. Lou, Z. Wang, X. Meng, Y. Liu, X. Qin, X. Zhang, Y. Dai, *Dalton Trans.* **43**, 8170 (2014)
10. X. Shi, P. Wang, L. Wnag, Y. Bai, H. Xie, Y. Zhou, L. Ye, *Appl. Catal. B* **243**, 322 (2019)
11. Y. Bai, X. Shi, P. Wang, L. Wnag, K. Zhang, Y. Zhou, H. Xie, J. Wang, L. Ye, *Chem. Eng. J.* **356**, 34 (2019)
12. X. Zhang, X. Liu, C. Fan, Y. Wang, Y. Wang, Z. Liang, *Appl. Catal. B Environ.* **132**, 332 (2013)
13. Y. Bai, L. Ye, T. Chen, P. Wang, L. Wang, X. Shi, P.K. Wong, *Appl. Catal. B Environ.* **203**, 633 (2017)
14. X. Cao, Z. Lu, L. Zhu, L. Yang, L. Gu, L. Cai, J. Chen, *Nanoscale.* **6**, 1434 (2014)
15. H. Cheng, B. Huang, Y. Dai, *Nanoscale* **6**, 2009 (2014)
16. P. Wang, B. Huang, X. Qin, X. Zhang, Y. Dai, J. Wei, M.H. Whangbo, *Angew. Chem. Int. Ed.* **47**, 7931 (2008)
17. D. Zhang, M. Wen, B. Jiang, G. Li, C. Jimmy, *J. Hazard. Mater.* **211**, 104 (2012)
18. J. Cao, B. Xu, H. Lin, B. Luo, S. Chen, *Chem. Eng. J.* **185**, 91 (2012)
19. C. Yu, F. Cao, G. Li, R. Wei, C.Y. Jimmy, R. Jin, Q. Fan, C. Wang, *Sep. Purif. Technol.* **120**, 110 (2013)
20. Y. Chang-Lin, Z. Wan-Qin, J.C. Yu, *Chin. J. Inorg. Chem.* **27**, 2033 (2011)
21. X. Zhang, Z. Ai, F. Jia, L. Zhang, *J. Phys. Chem. C* **112**, 747 (2008)
22. H. Liu, J. Xu, Y. Li, Y. Li, *Acc. Chem. Res.* **43**, 1496 (2010)
23. R.X. Wang, J.J. Fan, Y.J. Fan, J.P. Zhong, L. Wang, S.G. Sun, X.C. Shen, *Nanoscale* **6**, 14999 (2014)
24. R. Rahimi, S. Zargari, A. Yousefi, M. Yaghoubi-Berijani, A. Ghaffarinejad, A. Morsali, *Appl. Surf. Sci.* **355**, 1098 (2015)
25. M. Yao, Y. Meng, X. Mao, X. Ning, Z. Zhang, D. Shan, J. Chen, X. Lu, *Electrochim. Acta* **282**, 575 (2018)
26. C. Yu, C. Fan, X. Meng, K. Yang, F. Cao, X. Li, *React. Kinet. Mech. Catal.* **103**, 141 (2011)
27. R. Rahimi, M. Yaghoubi-Berijani, S. Zargari, M. Rabbani, S. Shariatnia, *Res. Chem. Intermed.* **42**, 4697 (2016)
28. X. Xiao, C. Liu, R. Hu, X. Zuo, J. Nan, L. Li, L. Wang, *J. Mater. Chem.* **22**, 22840 (2012)
29. R. Saraf, C. Shivakumara, S. Behera, N. Dhananjaya, H. Nagabhushana, *RSC Adv.* **5**, 9241 (2015)
30. H. Cui, Y. Zhou, J. Mei, Z. Li, S. Xu, C. Yao, *J. Phys. Chem. Solids* **112**, 80 (2018)
31. F. Shen, L. Zhou, J. Shi, M. Xing, J. Zhang, *RSC Adv.* **5**, 4918 (2015)
32. O. Bajjou, A. Bakour, M. Khenfouch, M. Baitoul, E. Faulques, M. Maaza, *Synth. Met.* **221**, 247 (2016)
33. M. Aydin, *Vib. Spectrosc.* **68**, 141 (2013)
34. H. Zhang, C.G. Niu, S.F. Yang, G.M. Zeng, *RSC Adv.* **6**, 64617 (2016)
35. J. Zhang, J. Lv, K. Dai, C. Liang, Q. Liu, *Appl. Surf. Sci.* **430**, 639 (2018)
36. C. Xue, T. Zhang, S. Ding, J. Wei, G. Yang, *ACS Appl. Mater. Interfaces.* **9**, 16091 (2017)
37. W. Maisang, A. Phuruangrat, C. Random, S. Kungwankunakorn, S. Thongtem, O. Wiranwetchayan, S. Wannapop, S. Choopun, S. Kaowphong, T. Thongtem, *Mater. Sci. Semicond. Process.* **75**, 319 (2018)
38. Y. Geng, N. Li, J. Ma, Z. Sun, *J. Energy Chem.* **26**, 416 (2017)
39. S. Obregón, A. Caballero, G. Colón, *Appl. Catal. B Environ.* **117**, 59 (2012)
40. S. Zargari, R. Rahimi, A. Ghaffarinejad, A. Morsali, *J. Colloid Interface Sci.* **466**, 310 (2016)
41. M. Sun, Q. Zhao, C. Du, Z. Liu, *RSC Adv.* **5**, 22740 (2015)
42. W. Li, D. Li, J. Wang, Y. Shao, J. You, F. Teng, *J. Mol. Catal. A: Chem.* **380**, 10 (2013)
43. R. Kumar, M.S. Abdel-Wahab, M.A. Barakat, J. Rashid, N. Salah, A. Al-Ghamdi, *J. Taiwan Inst. Chem. Eng.* **69**, 131 (2016)
44. S.G. Kumar, K.K. Rao, *RSC Adv.* **5**, 3306 (2015)
45. X. Hao, J. Gong, L. Ren, D. Zhang, X. Xiao, Y. Jiang, F. Zhang, Z. Tong, *Funct. Mater. Lett.* **10**, 1750040 (2017)